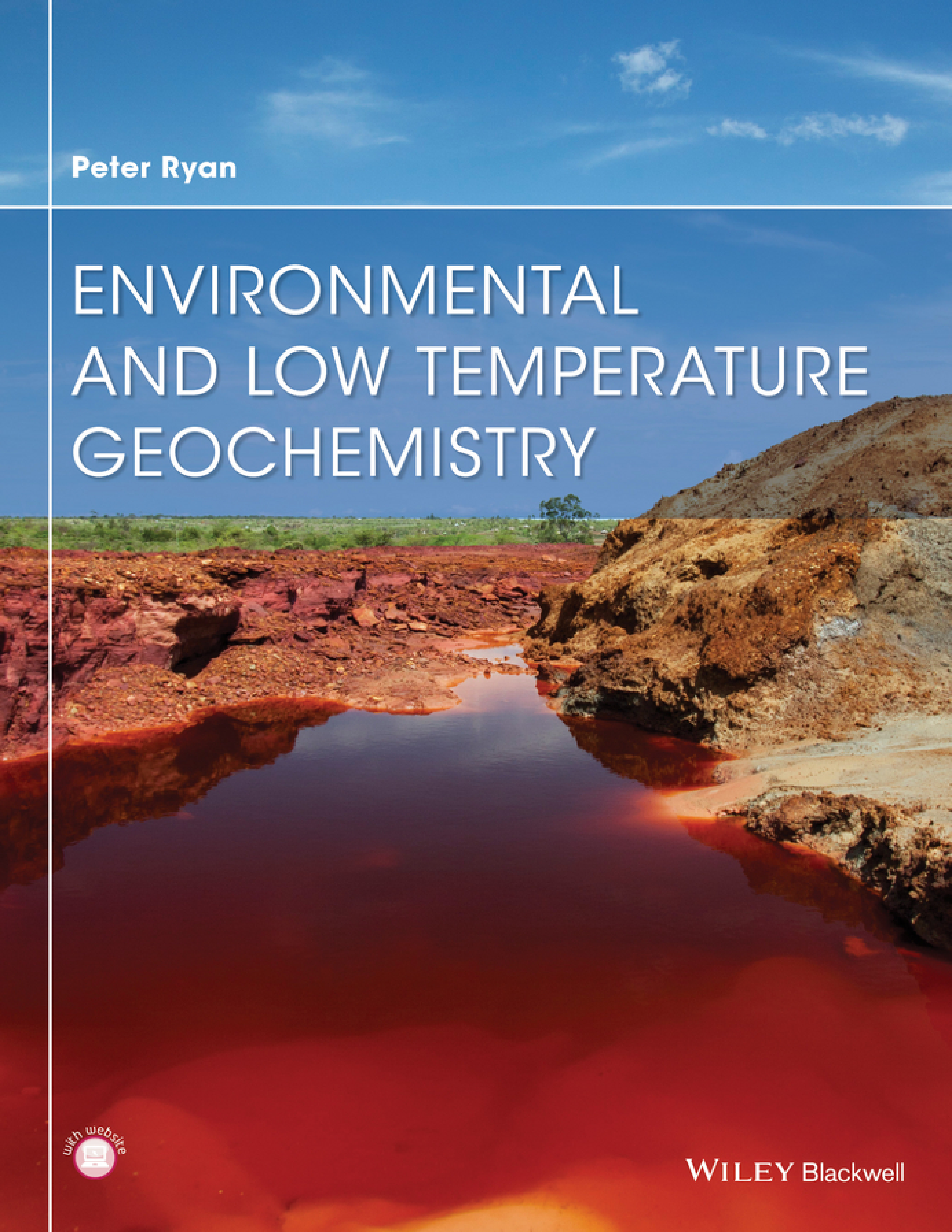

Peter Ryan

ENVIRONMENTAL AND LOW TEMPERATURE GEOCHEMISTRY

with website

WILEY Blackwell

CONTENTS

List of Tables

Chapter 01

Chapter 02

charge, first for common rock-forming minerals (O through Si), followed by heavy metals plus As, then other useful ions (S through U). Note that coordination number (CN) corresponds to geometry, i.e. CN of 4 produces tetrahedral geometry, CN of 6 produces octahedral geometry, CN of 8 produces cubic or dodecahedral geometry, and CN = 12 results in close-packed (CP) geometry, as explained in the text. Source: (Shannon 1976.)

Table 2.2 Composition of the Earth's crust presented as both wt% element (left) and wt% oxide (right). The difference between the sums listed and 100% reflects the abundance of all other elements.

Table 2.3 Classification of smectites based on octahedral occupancy and origin of 2:1 layers charge (i.e. octahedral vs. tetrahedral sheets).

Table 2.4 Isoelectric points and points of zero charge (PZC) of selected minerals (values = pH) and non-minerals. Note that isoelectric points and PZC values are very similar, but unlike isoelectric points, which are only a function of protonation and deprotonation, PZCs are also controlled by solution chemistry (e.g. adsorption–desorption of metals and other ions). At pH values below the isoelectric point, the mineral is an anion exchanger; above this value, the mineral sorbs cations.

Table 2.5 Cation-exchange capacities of selected minerals (note that oxyhydroxides are anion exchangers at pH values approximately < 7). These values were determined at pH = 7; values vary as a function of pH and aqueous composition. (Sparks 1995; Drever 1997; Langmuir 1997.)

Chapter 03

Chapter 04

Chapter 05

removed from the atmosphere is “Net sinks”. Also shown are percentages of fossil fuel and cement-derived C that remains in the atmosphere (increasing from 1960–2010), the amount of C sourced from fossils fuels and cement sequestered in the ocean (decreasing from 1960–2010), and total fossils fuels and cement sequestered (oceans + land; also decreasing with time).Table 5.4a Fluxes of carbon (Pg/yr). Negative values indicate reservoirs that are losing C.

Chapter 06

Table 6.1 Some common nitrogen species and the oxidation state of nitrogen in the compounds.

Table 6.2 Examples of sulfur species and the oxidation states of sulfur in these compounds, presented from most-reduced, S^{-2}-bearing species to the most-oxidized, sulfate-bearing species.

Chapter 07

Table 7.1 Concentrations of selected fixed gases in the atmosphere (sea level). Data are from Spiro and Stigliani (2006) and the Global Monitoring Division of the National Oceanic and Atmospheric Administration (USA) data on greenhouse gases. Data from Earth System Research Laboratory of US National Oceanic and Atmospheric Administration (http://www.esrl.noaa.gov/gmd/ccgg/trends/).

Table 7.2 Selected properties of greenhouse gases. Data are from Oak Ridge National lab (http://cdiac.ornl.gov/pns/current_ghg.html) and Forster et al. (2007).

Chapter 08

Chapter 09

Chapter 10

Chapter 11

List of Illustrations

Chapter 01

Figure 1.2 Schematic sketches of Bohr models of a carbon atom (^{12}C) showing, on the left, 6 protons and 6 neutrons in the nucleus with 6 electrons in 2 separate orbitals, and on the right, an atom that attempts to show the actual size of the nucleus compared to the electron cloud, yet even here the nucleus is ~100 times larger than an actual nucleus. The example on the right also introduces the idea of separate orbitals in the outer electron “shell”.

Figure 1.3 Lewis electron dot diagrams showing valence electrons of sodium and oxygen in their ground states (left) and in the compound Na_2O (right), where each sodium has lost an electron to oxygen, resulting in two Na^{+} and one O^{-2}.

Figure 1.4 Road sign in southwestern Ecuador.

Figure 1.5 Solubilities of ions as a function of ionic charge, from Inset 4 of *An Earth Scientist's Periodic Table of the Elements and Their Ions* (Railsback, 2003). Oxides of the elements are used as reference (e.g. lime, periclase, etc.). Note that low-charge base cations/alkali metals and cations of the alkaline Earth metals are relatively soluble, as are high-charge cations such as S^{+6} and N^{+5}, which form polytatomic anions (,). Cations with +3 and +4 charges (e.g. Al^{+3}, Ti^{+4}, Zr^{+4}) are insoluble in most surficial environments, with activities in H_2O at 25 °C of ~10^{-8} to 10^{-10}. (Railsback 2003.)

Figure 1.6 Schematic representation of formation of an ionic bond by transfer of the Na valence electron to Cl.

Figure 1.7 Lewis electron dot diagram of an oxygen molecule (O_2) shown using two different notations.

Note double bond between oxygen atoms consisting of two electron pairs depicted by the double dashed lines in the lower example.

Figure 1.8 Electronegativity of elements based on Linus Pauling’s early 20th-century research.

Figure 1.9 Plot of relationship between difference in electronegativity of two atoms in a bond and the percent ionic character of the bond. Note that no bond is 100% ionic; however, diatomic gases (e.g. N_2, Cl_2, O_2) and the C–C bonds in diamond are 100% covalent.. Based on early and middle 20th-century work of Linus Pauling and more recent research by Lu et al. (2006).

Figure 1.10 Diagram of three water molecules showing polarity of the water molecule (δ^+, δ^-) as well as hydrogen bonds (dashed lines) between H and O in adjacent molecules.

Figure 1.11 Van der Vaals bonds between adjacent atoms. A and B represent nuclei of adjacent atoms and dots are electrons. In the example on the left, electron clouds are shifted to the left, causing attraction of the atoms. In the example on the right, electron clouds are shifted to the right, also enhancing attraction of the atoms. If this type of alternating motion is synchronized, the atoms will be weakly attracted.

Figure 1.12 Typical progression of a geochemical system towards equilibrium. A high degree of disequilibrium in the early stages causes rapid rates of change, but as the system approaches equilibrium, rates decrease logarithmically.

Figure 1.13 Phase diagram for H_2O depicting one component (H_2O) and three phases (solid, liquid and gaseous water).

Figure 1.14 Schematic diagram illustrating relative stability conditions, from unstable at points A and C, to metastable at point B and stable at point D. Note that the metastable point B can be reached from points A or C, and that to shift from metastable (B) to stable (D), some energy must be introduced. If not, the metastable condition may persist for a long time.

Figure 1.15 Arrhenius plots showing relationship between equilibrium constant (K) and temperature for endothermic and exothermic reactions. For endothermic reactions, increasing temperature increases K, i.e. adding heat increases reaction rate; for exothermic reactions, the opposite is true.

Figure 1.16 Two graphical representations of zeroth (0^{th})-order chemical reactions, where [A] represents concentration of a chemical species (e.g. ion, mineral or compound). In the example on the left, decrease in concentration of A is linear, and on the right, the rate of change is constant.

Figure 1.17 Two graphical representations of first (1^{st})-order chemical reactions, where [A] represents concentration of a chemical species. On the left, change in concentration of A is logarithmic (solid line) or exponential (dashed line); on the right, for both cases (increasing or decreasing concentration), rate of change decreases in a linear fashion with time. Arrows in diagrams indicate direction of forward reaction (emphasizing that, on the right, the solid line represents decreasing [A] with time).

Chapter 02

occurrence of cations (e.g. Ca^{+2}, Mg^{+2}, Fe^{+2}, Na^{+}) in interstices. Larger sites mainly hold Na^{+} or Ca^{+2} whereas smaller sites hold Al^{+3} or Mg^{+2}.

Figure 2.13 Morphology of asbestiform amphibole (US Geological Survey Microbeam Lab; http://usgsprobe.cr.usgs.gov/picts2.html).

Figure 2.14 Arrangement of silica tetrahedra in phyllosilicates, showing laterally extensive development of sheet-like structures. This diagram shows a top-down view onto a tetrahedral sheet of a phyllosilicate.

Figure 2.15 Sketches of octahedral coordination of anions (typically O^{-2} or OH^{-}) around a cation (black). Anions are gray and white to allow the viewer to correlate the basal plane (gray spheres) to the upper plane (white spheres).

Figure 2.16 Two representations of a mica, both showing tetrahedral and octahedral sheets as well as interlayer potassium. (Adapted from Moore and Reynolds 1997.)

Figure 2.17 Schematic of pyrophyllite (left) and talc (right). Note (a) substitution of 3 Mg (talc) for 2 Al (pyrophyillite) in octahedral sheet, and (b) absence of interlayer cations in both.

Figure 2.18 Schematic sketches of mica and pyrophyllite. Note effect of presence/absence of interlayer potassium on the thickness of the unit cells in the – * direction.

Figure 2.19 Chlorite (left) and a 1:1 phyllosilicate (e.g. serpentine or kaolinite). Note that the interlayer in chlorite is an octahedral sheet, and that both chlorite and 1:1 phyllosilicates consist of alternating octahedral and tetrahedral sheets, the difference being the orientation of every other tetrahedral sheet.

Figure 2.20 The two ways that serpentines deal with the “mismatch problem”. On the left, the slightly larger octahedral sheet in chrysotile is draped over the curved tetrahedral sheet, ultimately forming rolled fibers. In antigorite (on the right), the mismatch is solved by short-period alternations (often of ~17 tetrahedra in length) of tetrahedral and octahedral sheets.

Figure 2.21 Rolled tetrahedral and octahedral sheets viewed down long axis of chrysotile from a transmission electron microscope image(A) (Yada 1971. Reproduced with permission from IUCR.) and fibrous white chrysotile on a serpentine rock surface(B).

Figure 2.22 Sketch of potassium feldspar showing potassium ions and silica tetrahedra. Gray triangles represent silica tetrahedral whose apices point away from the viewer. Note also that ¼ of tetrahedral sites are occupied by Al.

Figure 2.23 Two smectite 2:1 layers with hydrated cations (black spheres) occupying the interlayer site. Layer charge on each of the 2:1 layers (T–O–T) is −0.2 to −0.5 and this negative charge attracts cations to the interlayer. Variability in *c*-axis spacing is due to ability to intercalate different amounts of interlayer water (where the water is bonded to cations).

Figure 2.24 The transition from smectite to illite via interstratified illite/smectite, including the ordered I/S phase rectorite, a mineral in which illite and smectite layers alternate in an ordered manner. In sedimentary basins, this transition typically takes place progressively with increasing burial over the temperature range of 50 °C to 200 °C.

Figure 2.25 Schematic representation of the differences in cation exchange between kaolinite and smectite. “LC” indicates layer charge, which is zero in kaolinite but is −0.2 to −0.5 per unit cell in smectite. CEC of smectites is also enhanced by expandable interlayer spaces and smaller crystal size (not shown here).

Figure 2.26 Sketch of a goethite surface in solutions at pH = 5 (left) and pH = 9 (right), demonstrating the effect of IEP or PZC on ion-exchange capabilities of soil solids. Note the occurrence of anionic arsenate as inner sphere complex at pH = 5 (facilitated by H^{+}) compared to the occurrence of Ca^{+2} as an inner sphere complex at pH = 9. Negative signs near the goethite surface indicate a net negative charge at the mineral surface.

Figure 2.27 Molecule of calcite. Note rhombohedral structure that is also expressed in macroscopic crystals. Lines between oxygen atoms are used to indicate individualmolecules within the mineral structure.

Figure 2.28 Schematic diagram of sulfate (left) and sulfide (right) anions, with S ions drawn to scale (the radius of S^{-2} is approximately six times greater than S^{+6} in tetrahedral coordination).

Figure 2.29 Salts on dessicated shoreline of Salt Creek, Death Valley, USA. The white crusty coating is halite and other soluble salts precipitated at the surface when evaporation caused solute

Chapter 03

(PCBs). The numbered sites on the left correspond to potential bonding sites of functional groups (in PCBs, mainly H or Cl, sometimes OH). The example on the right is 3,3′,5,5′-tetrachlorobiphenyl.

Fig. 3.14 2,3,7,8-tetrachlorodibenzo-*p*-dioxin (TCDD), a member of the dioxins. Sites labelled with 1, 4, 6 and 9 are occupied by H.

Fig. 3.15 Structural formula of 2,4-dichloroethylene. Note the carboxyl (COOH) functional group in the upper right of the diagram and two Cl functional groups.

Fig. 3.16 Structural formula of glyphosate, known as N-(phosphonomethyl) glycine in IUPAC nomenclature. Note carboxyl group (far left), amine group (center), and phosphate (far right).

Fig. 3.17 Structural formula of malathion, which is known as O,O-dimethyl dithiophosphate or diethyl mercaptosuccinate in IUPAC nomenclature. Note the numerous functional groups, including methyl (CH_3), phosphate with sulfide in place of an O atom (thiophosphate), and esters (region with O double bonded to C–O).

Fig. 3.18 Methyl tert-butyl ether (MTBE), or 2-Methoxy-2-methylpropane according to IUPAC nomenclature.

Fig. 3.19 Top = structural formulas of bisphenol-A (top), known as BPA and also as 4,4'-(propane-2,2-diyl)diphenol in IUPAC nomenclature. Bottom = structural formula of estradiol, also known in IUPAC nomenclature as (17β)-estra-1,3,5(10)-triene-3,17-diol.

Fig. 3.20 Plot of log (K_{OW}) against log (bioconcentration factor, BCF), showing trend for a range of organic compounds in middle trophic level species (BCF generally increases with trophic level). Note the linear relationship for most of the plot (decreasing solubility in water = increased BCF), and the curious dip at high values of K_{OW}. Created from data in Banerjee and Baughman (1991) and Arnot and Gobas (2006).

Fig. 3.21 Correlation between the solubility in water (presented as log S^w, the aqueous solubility) and octanol–water coefficient (presented as log K_{OW}) of organic compounds. Low-solubility compounds such as DDT and PCBs plot in the upper left of the line and relatively soluble compounds such as benzene, PCE and 2,4-D plot in the lower right of the line. (Data from Chiou et al. 1977, 2005.)

Fig. 3.22 Formation of 2,4-D anion by deprotonation. The resulting anion may be sorbed to anion exchange sites.

Fig. 3.23 Isotherms describing chemisorptions (left) and physisorption (right) or organic compounds.

Fig. 3.24 Schematic diagram of behavior of NAPLs in the subsurface. Shown are two leaking underground storage tanks (USTs). Triangles indicate water table. The scale of the diagram does not permit depiction of sorption in the soil (refer to Chapter 9, Section 9.8).

Fig. 3.25 Decomposition of trichloroethylene (TCE) to the metabolite DCE, then to the metabolite vinyl chloride, under (most likely) microbially mediated reducing conditions and. Decomposition of vinyl chloride to the metabolite chloroethylene oxide tends to occur rapidly via microbial mediation in aerobic (oxidizing) waters but very slowly in anaerobic waters, and thus may persist in groundwater for years or decades.

Chapter 04

Fig 4.1 Hydrologic cycle with volumes of reservoirs given in units of km^3 and *fluxes* shown in units of km^3/year. Surface water as shown above refers to fresh water on the continents, and the overwhelming majority of this reservoir is accounted for in a few large lakes. Also, less than one-half of groundwater is accessible for use by humans; some is too deep and salty. (Modified from Winter et al. 1998.)

Fig 4.2 The white deposits surrounding the shallow pond in the foreground are evaporite salts that crystallized because evaporation of spring water raised dissolved ion concentrations to saturation. Evaporite minerals in this area include halite, gypsum, calcite and borax. Death Valley, USA. (Courtesy of the US Geological Survey.)

Fig 4.3 Sketch showing, from top to bottom, the vadose zone (unsaturated zone), which includes soil and any sediment or rock above the water table) and the shallow part of an aquifer (the saturated zone). Connections between groundwater and surface water are also shown by arrows indicating, typical groundwater flow paths. Relative total dissolved solids (TDS) of precipitation, soil water, groundwater and surface water for a temperate region are shown.

Fig 4.4 Changes in the ratio of Na/(Na + Ca), based on units of mass (e.g. mg/L), plotted against total dissolved solids (TDS, in mg/L), for streams from different climate zones, and also for seas and oceans. Arrows indicate changes in stream composition that occur progressively downstream; for example, with increasing contributions from chemical weathering, tropical soils increase in TDS and the Na/(Na + Ca) ratio decreases. (Modified from Gibbs 1970 and Andrews et al. 2004.)

Fig 4.5 The structure of the H_2O molecule. (A) emphasizes the tetrahedral nature of the molecule, and (B) and (C) show the structure and dipolar nature in two dimensions.

Fig 4.6 Schematic sketch of the relationship of polar water molecules to a sodium cation (above) and chloride anion (below) in solution.

Fig 4.7 Hydrogen bonds (dashed lines) between adjacent water molecules.

Fig 4.8 Decreasing rate of dissolution of a mineral (e.g. sodium feldspar) in a closed system as measured by the concentration of a dissolved constituent (e.g. $Na^{\pm}$) released during dissolution. Note that concentration in solution increases until the solution reaches saturation, at which time the system reaches dynamic equilibrium. In an open system, leaching of $Na^{\pm}$ would likely prevent attainment of dynamic equilibrium. In terms of residence time, the concentrations of dissolved constituents will increase with time in this type of example.

Fig 4.9 Prediction of solubility of aqueous ions based on the ratio of ionic charge (z) to ionic radius (r, in Å), a ratio known as ionic potential. In the case of polyatomic molecules (e.g. H_4SiO_4), radius (r) is for the elemental ion shown (e.g. $Si^{\pm 4}$), not for the entire molecule. The z values on both upper and lower x-axes are absolute values, and the y-axis data are based on concentrations in river water determined by

Martin and Whitfield (1983); the plot shown is based on a graph in Andrews et al. (2004).

Fig 4.10 Solid curve is sum of all dissolved Al species and dashed lines correspond to Al species indicated. Note low solubility of Al between pH = 6 to 7 and exponential increase in solubility with decreasing or increasing pH.

Fig 4.11 Structural formula of ethylenediaminetetraacetate (EDTA) molecule, a good example of a chelating compound.

Fig 4.12 Approximate locations of selected natural systems as a function of reduction–oxidation potential and pH. Note that redox units are given in terms of Eh (left) and p*e*. The thin line bounding the natural environments indicates the limits of nearly all natural waters (after Bass Becking et al. 1960).

Fig 4.13 Copper and lead Eh–pH diagrams at 25 °C and 1 atm pressure. Activities of Cu and Pb are 10^{-6} mol/L, pCO_2 = 400 ppmv ($10^{-3.4}$ atm) and total S = 10^{-2} mol/L.

Fig 4.14 Arsenic and uranium Eh–pH diagrams for systems at 25 °C and 1 atm pressure. For the arsenic diagram, activity of $As_{total} = 10^{-6}$ and S activity = 10^{-2} mol/L. For the uranium diagram, activity of U = 10^{-8} mol/L and C (as CO_2) is $10^{-3.4}$ atm.

Fig 4.15 Eh–pH diagram for iron and aluminum. For the iron diagram, activity of Fe = 10^{-6} mol/L, S = 10^{-2} mol/L and $CO_2 = 10^{-3.4}$ atm. For aluminum diagram, Al = 10^{-9} mol/L. Note that iron speciation is influenced by both Eh and pH; conversely, aluminum speciation is controlled by pH but not Eh. The arrow from A to B represents oxidation as shown in Plate 5.

Fig 4.16 Solubility of silica as a function of pH in equilibrium with amorphous silica and with quartz. Note that if amorphous silica is the solid phase in equilibrium with silica, dissolved silica concentrations are approximately an order of magnitude greater than when quartz controls silica solubility.

Fig 4.17 Adsorption of metal cations onto ferrihydrite as a function of pH. Data are from Dzombak and Morel (1990) except for uranyl, which is from Hsi and Langmuir (1985). The curvature in the adsorption edges indicate that, at low pH, adsorption is relatively weak; with increasing pH, cations are more-strongly adsorbed. For example, at pH = 4, Cu^{+2} is weakly adsorbed (i.e. only a small proportion of Cu^{+2} ions in solution will be adsorbed at pH = 4), but at pH = 5.5, nearly all Cu^{+2} in solution will be adsorbed onto ferrihydrite. The boundary between pH 4 and 5.5 is the adsorption edge for Cu^{+2}.

Fig 4.18 Adsorption of the polyatomic anions selenate, sulfate, chromate, arsenite () and arsenate () onto ferrihydrite as a function of pH. Data are from Dzombak and Morel (1990). Note that for all anions shown but arsenite, the shape of the curve is the inverse of the curves for metal cations shown in Fig. 4.19, reflecting the fact that, as pH decreases, surfaces of ferrihydrite become progressively more occupied by H^{+}, creating positive surface charge needed for adsorption of anions. Thus, adsorption increases to the left of this diagram. Although not shown, decreasing pH causes protonation of the anions (e.g. toto ,toto , etc.).

Fig 4.19 Adsorption isotherms. A = linear isotherm, B = Langmuir isotherm and C = Freundlich isotherm. The *x*-axis is activity of sorbate (e.g. ion) and y-axis is